PNAS RESEARCH ARTICLE | CHEMISTRY

A first principles analysis of potential-dependent structural evolution of active sites in Fe-N-C catalysts

Ankita Morankar[a], Siddharth Deshpande[a], Zhenhua Zeng[a], Plamen Atanassov[b], and Jeffrey Greeley[a,1]

Edited by Manos Mavrikakis, Cornell University, Ithaca, NY; received May 19, 2023; accepted October 10, 2023 by Editorial Board Member Sharon Hammes-Schiffer

Fe-N-C (iron–nitrogen–carbon) electrocatalysts have emerged as potential alternatives to precious metal-based materials for the oxygen reduction reaction (ORR). However, the structure of these materials under electrochemical conditions is not well understood, and their poor stability in acidic environments poses a formidable challenge for successful adoption in commercial fuel cells. To provide molecular-level insights into these complex phenomena, we combine periodic density functional theory (DFT) calculations, exhaustive treatment of coadsorption effects for ORR reaction intermediates, including O and OH, and comprehensive analysis of solvation stabilization effects to construct voltage-dependent ab initio thermodynamic phase diagrams that describe the in situ structure of the active sites. These structures are further linked to activity and stability descriptors that can be compared with experimental parameters such as the half-wave potential for ORR and the onset potential for carbon corrosion and CO_2 evolution. The results indicate that pyridinic Fe sites at zigzag carbon edges, as well as other edge sites, exhibit high activity for ORR compared to sites in the bulk. However, edges neighboring the active sites are prone to instability via overoxidation and consequent site loss. The results suggest that it could be beneficial to synthesize Fe-N-C catalysts with small sizes and large perimeter edge lengths to enhance ORR activity, while voltage fluctuations should be limited during fuel cell operation to prevent carbon corrosion of overoxidized edges.

fuel cells | oxygen reduction reaction | Fe-N-C catalysts | density functional theory

Significance

The ongoing search for fuel cell catalysts has focused on reducing the content of platinum group metals (PGMs). PGM-free catalysts, composed of metal ions, nitrogen atoms, and graphene-like carbon matrices, are low cost and provide reasonable activity. However, they are degraded in acidic environments, and this process is poorly understood. Here, we use theory to elucidate the molecular details of the activity and stability of Fe-N-C catalysts. Fe sites at graphene edges exhibit high activity for ORR in comparison with Fe sites in the bulk, but these edges are prone to over-oxidation and consequent activity loss. The results suggest that an inherent tradeoff exists between catalytic activity and stability for these PGM-free electrocatalysts.

Iron–nitrogen–carbon catalysts (Fe-N-C) (1–4) have recently emerged as potential alternatives (5) to platinum group-based materials (PGM) for use as electrocatalysts in carrying out the electrochemical conversion of oxygen to water in proton exchange membrane hydrogen fuel cells (6–8). A significant limitation of these catalysts, however, is that their activity declines over time. Numerous site degradation mechanisms, such as oxidative attack by hydrogen peroxide (9, 10), carbon corrosion (11–13), dissolution of iron (11, 14), and anion adsorption blocking active sites (15), have been proposed as possible explanations for the activity loss, with some indications that the deactivation mechanism may be dependent on the applied potential. However, these processes are not well understood at the molecular level, and an improved understanding of the underlying structure of the catalyst could help to both shed light on these mechanisms and, ultimately, develop strategies for enhancing catalyst performance.

A significant challenge in successfully understanding reactivity at the molecular scale stems from the difficulty of controlling and characterizing the active site structures in Fe-N-C catalysts. Synthesis with high-temperature pyrolysis leads to a distribution in FeN_x (x: 1-4) moieties and nitrogen defects that are dispersed in different porous structures in the carbon matrix of graphene. The exact coordination and atomic environment of the metal-containing centers in FeN_x moieties are still debated due to these structural variations (16). For example, experimental studies have provided direct spectroscopic evidence for the presence of single FeN_4 sites with scanning transmission electron microscopy (STEM) and complementary electron energy loss spectra (EELS) (17), but other types of FeN_x sites (FeN_3, FeN_2) and nitrogen groups have likewise been identified with X-ray photoelectron spectroscopy (XPS) (16). Among these disparate moieties, FeN_x sites are thought to be major contributors to the ORR compared to nitrogen defects (18) or residual iron nanoparticles (11, 19). Mossbauer spectroscopy studies, in combination with theoretical calculations, have additionally been used to assign FeN_x moieties either to pyrrolic FeN_4 sites located in pores (20, 21) or in the bulk of graphene sheets (22), or to pyridinic FeN_4 sites in the bulk (20, 21). The above studies, in conjunction with CO cryochemisorption and nitrite reduction stripping, have been used to quantify site densities in catalysts prepared by different synthesis protocols (23). Further, computational studies with density

Author affiliations: [a]Davidson School of Chemical Engineering, Purdue University, West Lafayette, IN 47907; and [b]Chemical & Biomolecular Engineering and National Fuel Cell Research Center, University of California, Irvine, CA 92617

Author contributions: P.A. and J.G. designed the research; A.M. performed the research; A.M., S.D., and Z.Z. analyzed data; and A.M. wrote the paper.

The authors declare no competing interest.

This article is a PNAS Direct Submission. M.M. is a guest editor invited by the Editorial Board.

[1]To whom correspondence may be addressed. Email: jgreeley@purdue.edu.

This article contains supporting information online at https://www.pnas.org/lookup/suppl/doi:10.1073/pnas.2308458120/-/DCSupplemental.

Published November 29, 2023.

functional theory (DFT) have found that pyridinic FeN_4 sites have the most thermodynamically favorable formation energies, followed sequentially by pyridinic FeN_3 and FeN_2 sites (24, 25). It has also been reported that pyridinic FeN_4 and FeN_3 moieties in close proximity to one another, at a zigzag edge of graphene, have accessible formation energies (26). The large variability in molecular-level structures demonstrated in the above studies makes determination of the site having the highest intrinsic ORR activity and stability very challenging. Such determinations are further complicated by the fact that some moieties or site features are likely to be invisible to spectroscopic and microscopic techniques if present in low concentrations, but they could nevertheless contribute significantly to the overall reaction rates if their intrinsic reactivity is high. These considerations have led us to expand our active site models beyond those proposed in experiments, and we therefore undertake an extensive comparison of different active site candidates.

In addition to the wealth of active site structures in the Fe-N-C catalysts induced by pyrolytic synthesis, in situ structural transformations can occur under reaction conditions, leading to additional complexities in predicting and understanding the activity and stability of these sites. To provide insights into the molecular-level structures of Fe-N-C catalysts, their in situ transformations, and the associated catalytic performance, we introduce a comprehensive computational approach to assess the thermodynamic characteristics of these materials. Structural features are determined for possible active site geometries as a function of applied electrode potential using ab initio phase diagram analyses. These phase diagrams incorporate both adsorbate–adsorbate interactions at high mixed coverages of ORR intermediates and coverage-dependent adsorbate–solvent interactions. These effects have received little attention in the context of Fe-N-C catalysts but nonetheless play a vital role in providing in situ structural insights.

Numerous active site configurations are explored, assessing the effects of variation in site location within a single graphene layer, site clustering, and nitrogen coordination on their propensity for oxidation and their catalytic activity. The structural evolution is, in turn, tied to the site's activity and stability using the limiting potential, U_L, and the overoxidation potential, U_O, as theoretical descriptors. The limiting potential is defined as the potential at which an active site is poisoned and can no longer turn over reaction intermediates for the ORR. Hence, this descriptor reflects the potential range for the activity of a given site configuration and can be compared with the experimentally observed activity for the Fe-N-C catalyst. The latter is expressed in terms of the half-wave potential, $E_{1/2}$, which is defined as the potential corresponding to half of the diffusion current observed in polarization curves under mass transfer limitations. This metric is often used to compare activities of ORR electrocatalysts, with those exhibiting values closest to the theoretical redox potential ($E_{ORR} = 1.23\,V$) being the most active. In turn, comparing calculated site activities, in the form of U_L, with the experimentally measured $E_{1/2,\,Fe-N-C} \sim 0.85\,V$ values, provides insights into the active sites responsible for the ORR. The overoxidation potential, on the other hand, is defined as the potential at which carbon atoms neighboring the FeN_x active sites start becoming occupied by OH and O intermediates. This potential is used as a thermodynamic stability indicator for catalyst degradation via a carbon corrosion mechanism and is compared with the experimentally observed onset potential for $CO_{2\,(g)}$ species ($E_{CO_2\,onset} = 0.90\,V$) (11). Overoxidation of carbon atoms adjacent to the active sites is undesirable at conditions close to the ORR operating potential due to the possibilities of the oxides inducing deactivation of the FeN_x sites and of carbon corrosion being initiated at the overoxidized regions and leading to site loss. Higher values of U_O are therefore associated with higher intrinsic site stabilities.

The site-dependent structure–activity–stability analyses provide useful insights into the molecular-level factors that govern the stability and activity of PGM-free electrocatalysts. We expect that these insights will, ultimately, point to design principles for Fe-N-C catalysts, permitting targeted synthesis of materials with improved catalytic properties.

Results

All active site configurations considered in this work are illustrated in Fig. 1. Both 6-membered pyridinic (Fig. 1 *A–C*) and 5-membered pyrrolic nitrogen (Fig. 1 *D–F*) rings are analyzed. The location of the pyridinic FeN_4 site is considered in the bulk of a graphene sheet (also called an in-plane defect), at a graphene armchair edge, and at a zigzag edge, while the location for the pyrrolic FeN_4 site is in either the bulk of a graphene sheet or between graphitic pores of varying sizes. The effect of FeN_x clustering is studied by comparing two FeN_4 sites with carbon atoms separating them (Fig. 1*G*) to a bimetallic Fe_2N_6 cluster (Fig. 1*H*). Finally, the effect of nitrogen coordination is studied by comparing Fe_2N_6 (Fig. 1*H*) and Fe_2N_5 clusters (Fig. 1*I*).

Active Site Structures from Ab Initio Thermodynamic Phase Diagrams. To predict the structure of the various Fe-N-C sites as a function of the electrode potential, we generate a series of ab initio phase diagrams. For a given Fe-N-C site type, we exhaustively enumerate all possible arrangements of hydroxyl (OH) and epoxy (O) groups at multiple coverages, using a graph theory–based geometric algorithm termed SurfGraph (27), and we estimate the free energy, ΔG, of their respective arrangements, as follows:

$$\Delta G = \Delta E + \Delta ZPE - T\Delta S + \Delta E_{solv}. \quad [1]$$

ΔE is the binding energy for a given adsorbate, defined as the reaction energies of their corresponding reactions, and is taken from DFT calculations.

$$H_2O + * \leftrightarrow OH^* + (H^+ + e^-), \quad [2]$$

$$H_2O + * \leftrightarrow O^* + 2\left(H^+ + e^-\right). \quad [3]$$

Here, H_2O is in the gas phase, and $(H^+ + e^-)$ is related to H_2 in the gas phase using the computational hydrogen electrode scheme. The effect of a bias on all states involving a coupled proton–electron transfer step is included by shifting the free energy of this state by –eU, where U is the electrode potential on an RHE scale (28). Further, ΔZPE is the zero point energy difference, while ΔS is the change in the entropy corresponding to a given reaction. These values have been taken from previous reports and standard tables for gas phase molecules and are listed in *SI Appendix*, Table S1. Finally, ΔE_{solv} is the solvation stabilization experienced by the adsorbate, which is determined using a modified ab initio molecular dynamics routine for OH adsorbates. For a given voltage, the state with the lowest free energy is taken as the thermodynamically preferred configuration.

We now discuss the construction and interpretation of the phase diagrams, including the voltage-dependent in situ structural implications for site activity and site stability, for a subset of the active sites in Fig. 1. These sites include pyridinic structures at varying locations in the graphene sheets (Fig. 1 *A–C*) and with

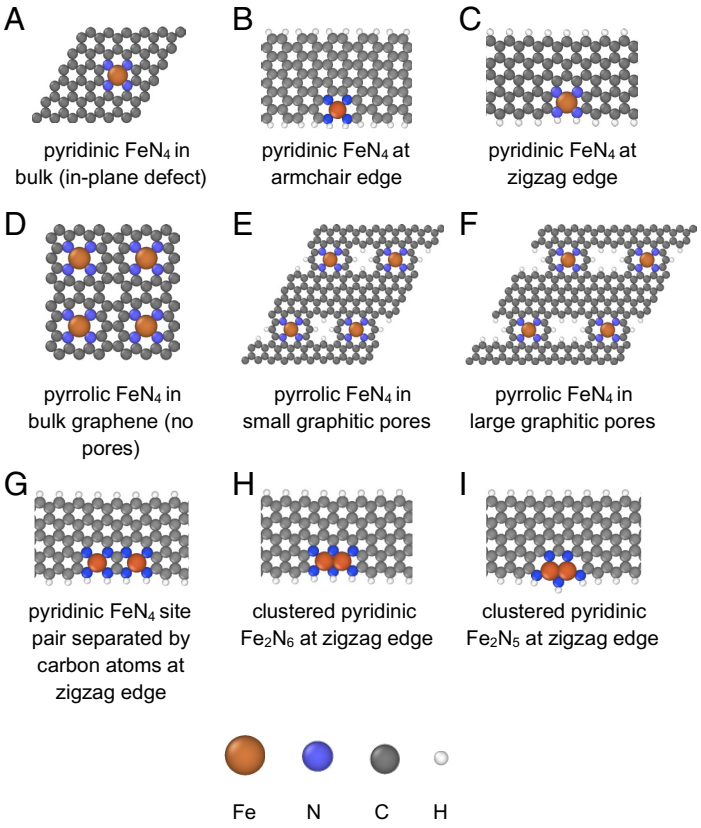

Fig. 1. Structures for unit cells of FeN_4 active sites in different configurations. (*A–C*) FeN_4 with nitrogen in six-membered pyridinic rings, (*D–F*) FeN_4 with nitrogen in five-membered pyrrolic rings (unit cell is repeated twice in x and y directions), (*G*) pyridinic FeN_4 site pair at zigzag edge of graphene separated by carbon atoms, (*H*) clustered pyridinic Fe_2N_6 site at the zigzag edge of the graphene sheet, and (*I*) clustered pyridinic Fe_2N_5 site at the zigzag edge of the graphene sheet.

different clustering of Fe moieties (Fig. 1 *G* and *H*). These cases are chosen to capture key performance trends, but similar analyses have been performed for the pyrrolic site configurations (Fig. 1 *D–F*) and clustered Fe_2N_5 (Fig. 1*I*) configurations, as well, and they are included in *SI Appendix*, section S3. The structural evolution is analyzed in a voltage window between 0 V and the thermodynamic redox potential for ORR, 1.23 V. We note that the resulting thermodynamic interpretations are applicable to both acidic and alkaline pH conditions, as we use an RHE potential scale.

Pyridinic FeN_4 in Bulk (In-Plane Defect). The phase diagram for a pyridinic FeN_4 site located in the bulk of a graphene sheet (Fig. 1*A*) is shown in Fig. 2. The results indicate that the active site (structure 1, outlined in red) is oxidized with a single OH^* (structure 2, outlined in purple, where "*" represents Fe as the binding site) at 0.0 V on exposure to water. This configuration has the most favorable free energy up to a potential of 0.34 V, as represented by the purple region. We term this a spectator OH^* moiety, as it remains bound to the Fe on one side of the graphene sheet under the oxidizing potentials for ORR, but it does not deactivate the site. This result is consistent with previous reports (17). Since these passivating OH groups are ubiquitous in the Fe-N-C sites, we define the structure containing the spectator species to have a free energy of 0 eV in all subsequent phase diagrams in this work.

The vacant side of the FeN_4 site, opposite to the the spectator group, is the active phase where ORR occurs. Up to a potential of 0.34 V, there is a driving force for conversion of OH^* (structure 3 in green) to water, leaving a vacant site (structure 2 in purple) that may then undergo another ORR turnover cycle. Hence, this purple region is the potential window where ORR is active. Above 0.34 V, the OH^* binds too strongly to the active site and poisons it. This inactive region is indicated by the green shading in the phase diagram, and as discussed above, the onset potential for site poisoning is denoted as the thermodynamic limiting potential, U_L, which we use as the activity indicator for the ORR. Note that, although we report only an OH group as the spectator and poisoning species, other ORR intermediates are also analyzed, but they are not involved in the rate-limiting step, and hence, they do not appear among the most stable phases shown in the phase diagram (refer *SI Appendix*, section S3.1).

In addition to poisoning of the FeN_4 site with OH^* on both sides of the graphene sheet, we consider the possibility of OH or O adsorption on carbon and nitrogen atoms neighboring the iron atoms. This process is termed overoxidation, and the potential above which overoxidized structures are thermodynamically accessible is denoted as the thermodynamic overoxidation potential, U_O, which we use as the stability indicator for the catalyst during ORR. A rigorous screening of high and mixed coverage structures involving all unique combinations of hydroxy and epoxy intermediates, enumerated with SurfGraph (27), shows that the first carbon shell surrounding the FeN_4 site is most vulnerable to oxidation. On the other hand, the intermediates do not adsorb on the ligating nitrogens. The $OH^{\#}$-OH^*, $2OH^{\#}$-OH^*, and $O^{\#}$-OH^* (structures 4, 5, and 6, respectively, where # represents C as the binding site) are most stable among all high and mixed coverage structures considered, but they are thermodynamically more favorable than the Fe-poisoned OH^* (structure 3) only at very highly oxidizing conditions, beyond the potential range that we consider in this analysis. Hence, carbon atoms in the bulk surrounding in-plane pyridinic FeN_4 sites are quite stable and are unlikely to undergo overoxidation.

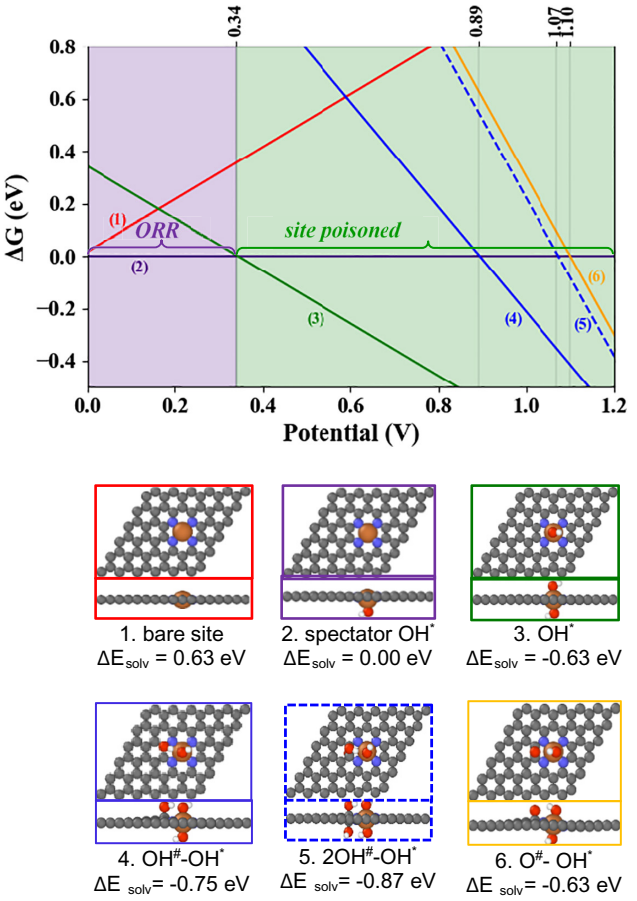

Fig. 2. Phase diagram for a pyridinic FeN_4 site in the bulk of graphene with corresponding oxidized site configurations having OH and O groups that are energetically referenced to H_2O (top and front views). Structure 1 (red) is the bare site configuration. Structures 2 to 6 have a spectator OH^* group. OH^* poisons the FeN_4 active site in structure 3 (green). Structures 4 to 6 have overoxidizing $OH^{\#}$, $2OH^{\#}$, and $O^{\#}$ groups, respectively, on carbon atoms surrounding FeN_4, in addition to OH^* on iron. The overoxidizing groups cluster around the FeN_4 site, forming intramolecular H-bonds. The outline colors for the configurations correspond to the colored lines and regions in the phase diagram. The potentials at which phase transitions occur are shown on the secondary *X* axis at the top of the diagram. Structure 2 is assigned a reference energy of 0 eV. Solvation correction values for every configuration are listed with respect to the reference structure 2. Free energies for phase transitions for every other structure by exchange of water, protons, and electrons are calculated with respect to this reference phase.

We note that the aqueous solvation effects, mentioned above, often lead to significant stabilization of the various surface structures. As an example, an OH^* on Fe (structure 3) is found to be stabilized by H-bonding with water by −0.63 eV, while an $OH^{\#}$ on carbon is stabilized by −0.43 eV. Considering such solvation effects explicitly is of utmost importance, as they may lead to shifts in the predicted limiting potentials and carbon oxidation potentials. Solvation stabilization is also dependent on the oxide coverage under consideration, as the existence of intramolecular H-bonding interactions among adsorbates in the clustered configurations (structures 4, 5, and 6, respectively) decreases their interactions with the surrounding solvent molecules. For example, the solvation for an $OH^{\#}$-OH^* pair (structure 4) is found to be −0.75 eV, significantly less than a solvation correction that would be obtained by considering simple addition of individual solvation contributions from OH^* and $OH^{\#}$ (−1.06 eV). We believe that these coverage and site identity–dependent solvation stabilization effects, which have not been rigorously considered in the past, provide useful additional information on catalyst stability and activity. We provide a detailed discussion on the solvation analysis in *SI Appendix*, section S4.2.1 and report solvation values specific to each configuration in Fig. 2.

In summary, we account for potential, coadsorbate, and solvent effects in building thermodynamic phase diagrams to track structural evolution of the pyridinic FeN_4 sites in the bulk of graphene. This site exhibits low intrinsic ORR activity due to poisoning at U_L = 0.34 V, although its resistance to carbon overoxidation is significant. The large difference between the calculated U_L and the measured $E_{1/2} \sim 0.85$V indicates that this is likely not the active site contributing to ORR in Fe-N-C catalysts.

Pyridinic FeN_4 at an Armchair Edge. We now consider the pyridinic FeN_4 active site at an armchair edge of a graphene sheet as an active site model (Fig. 1*B*). The phase diagram in Fig. 3 indicates that a spectator OH^* group forms on Fe at 0.16 V (structure 2 in purple). The onset potential for spectator formation is higher compared to the case of the bulk pyridinic FeN_4 site, which may be ascribed to a change in the electronic structure of the FeN_4 due to its altered coordination environment at the graphene sheet edge. Further increases in potential lead to poisoning of the active site with OH^* at 0.47 V (structure 3 in green), giving an ORR active potential window between 0.16 and 0.47 V, which constitutes a slight improvement in activity compared to its bulk counterpart. At higher voltages, overoxidation sets in, and formation of $2O^{\#}$-OH^* and $4O^{\#}$-OH^* groups is observed at 0.77 V and 1.00 V, respectively (structures 4 and 5 in solid and dashed yellow). In these structures, the carbon atoms along the armchair edge are observed to be more susceptible to overoxidation by epoxy groups occupying bridge positions (structures 4 and 5, outlined in yellow), as opposed to oxidation by hydroxy groups on top sites in a $4OH^{\#}$-OH^* structure (structure 6 in blue). We note that these structures are obtained after a rigorous screening of high and mixed coverage structures. The solvation stabilization for these structures is assumed from similar coverage structures for pyridinic sites in the bulk of graphene, with more details provided in *SI Appendix*, section S4.2.2.

The pyridinic FeN_4 site at an armchair edge is not a probable candidate for the ORR active site, given a significant difference of its activity, U_L = 0.47 V, from the measured $E_{1/2}$. If present in Fe-N-C samples, these structures could overoxidize above U_O = 0.77 V and may therefore be prone to degradation via carbon corrosion.

Pyridinic FeN_4 at Zigzag Edge. We next discuss the pyridinic FeN_4 active site at a zigzag edge (Fig. 1*C*). As seen in Fig. 4, this site forms a spectator OH^* group at 0.14 V (structure 2 in purple), similar to the case with the armchair edge. The ORR is active between 0.14 and 0.68 V, while OH^* poisons the site above U_L = 0.68 V (structure 3 outlined in green). Hence, site location along the zigzag edge greatly enhances activity towards ORR compared to the armchair edge, bringing the onset potential close to the experimentally measured $E_{1/2} \sim 0.85$V. We consider this result to be within the accuracy of our theoretical prediction, which is determined by standard errors in density functional theory calculations and by sampling uncertainties in the determination of solvation stabilization energies (~0.15 eV).

Similar to the case of the armchair edge, activity enhancement due to site location along a zigzag edge is coupled with carbon overoxidation at U_O = 0.79 V. The $OH^{\#}$-OH^* configuration (structure 5 in solid blue), with a neighboring carbon atom along the zigzag edge, is formed at this voltage, and it is closely followed by an even more heavily oxidized $4OH^{\#}$-OH^* state (structure 6 in dashed blue) at 0.80 V. In contrast to epoxy groups observed for armchair edges, the carbon atoms along the zigzag edge are prone to overoxidation by hydroxy groups. Compared to pyridinic FeN_4 in the bulk of graphene, these hydroxy groups are located

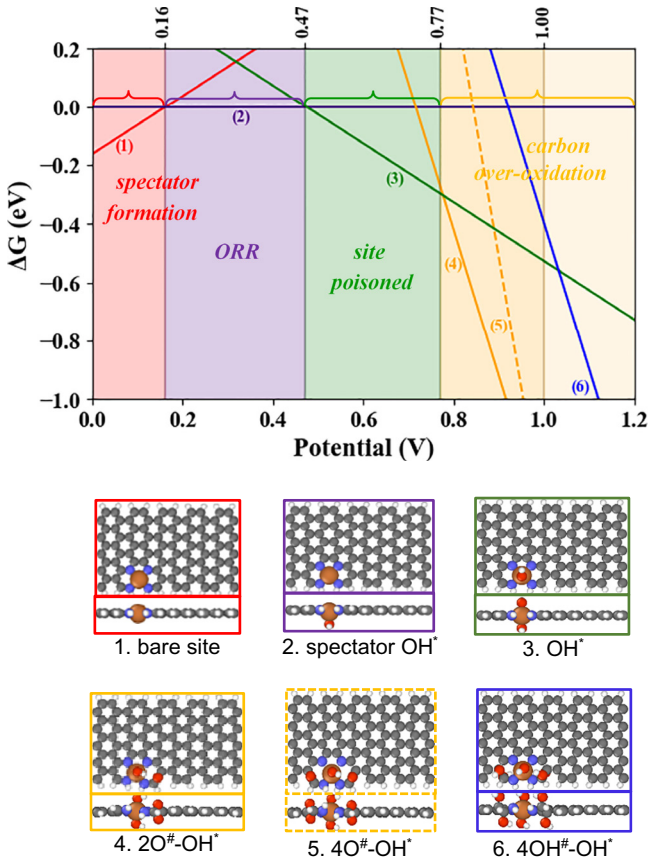

Fig. 3. Phase diagram for a pyridinic site at the armchair edge of graphene and oxidized site configurations having OH and O groups that are energetically referenced to H_2O (top and front views). Structure 1 is a bare FeN_4 site configuration. Structures 2 to 6 have a spectator OH^* group. OH^* poisons the FeN_4 active site in structure 3. Structures 4 to 6 have overoxidizing $2O^{\#}$, $4O^{\#}$, and $4OH^{\#}$ groups, respectively, on carbon atoms surrounding FeN_4, in addition to the OH^* on iron. The overoxidizing groups cluster around the FeN_4 site, forming intramolecular H-bonds. Structure 2 is assigned a reference energy of 0 eV. Free energies for phase transitions for every other structure by exchange of water, protons, and electrons are represented with respect to the reference phase with a single spectator OH* moiety.

further away from the FeN_4 site, such that intramolecular H-bonding is not always present between them. This is evident, for example, in structure 4, where the $OH^{\#}$ is far from the OH^* on the iron atom, with no H-bonding between the two, at a distance of ~4 Å. The $4OH^{\#}$-OH^* configuration, however, exhibits some degree of OH clustering, with two of the four $OH^{\#}$-OH^* pairs forming intramolecular H-bonds. The impact of solvation stabilization on these structures is discussed in *SI Appendix*, section S4.2.3.

Since pyridinic FeN_4 sites at the zigzag edge of graphene exhibit high intrinsic ORR activity, with U_L = 0.68 V, we propose that this may be an active site that contributes to ORR activity in Fe-N-C catalysts. However, these sites experience a close competition between ORR and deactivation by carbon overoxidation, which could initiate at voltages as low as U_O = 0.79 V.

Given the high activity of sites along the zigzag edge, we further explore the effect of site coupling to determine whether this effect can further enhance activity or stability. We begin with the case of a pair of pyridinic FeN_4 sites at the zigzag edge, separated by carbon atoms (Fig. 1*G*), and conclude with a pyridinic Fe_2N_6 cluster (Fig. 1*H*), both of which have been reported to have favorable formation energies from computational studies (26).

Pyridinic FeN_4 Site Pair Separated by Carbon at Zigzag Edge. Fig. 5 shows the phase diagram for the pyridinic FeN_4 site pair along a zigzag edge. We find that a spectator OH^* group forms on each of the iron atoms (structure 3 in purple) at 0.08 V. As the potential is increased, $2OH^*$ (structure 4 in green) forms at 0.77 V, where an OH^* intermediate forms on the second vacant side of each iron site. The iron sites are completely occupied by ORR intermediates in this structure, giving U_L = 0.77 V. Even higher coverages of overoxidized structures are also considered, where we note that carbon atoms separating the two FeN_4 sites are resistant to overoxidation, but carbon atoms on either side of the FeN_4 site become overoxidized. The $OH^{\#}$-$2OH^*$ structure (structure 5 outlined in solid blue), with an additional $OH^{\#}$ group along the zigzag edge compared to structure 4, forms at 0.73 V, giving U_O = 0.73 V. A further increase in potential leads to heavier overoxidation of the edge carbon atoms on either side of the FeN_4 pair, ultimately forming a $4OH^{\#}$-$2OH^*$ structure (structure 6 in dashed blue).

We note that, in the previously discussed cases for single FeN_4 sites, carbon overoxidation is observed to occur at potentials higher than the potential of iron site poisoning ($U_O > U_L$). However, in this case, the propensity for carbon overoxidation is so high that it induces deactivation by causing site poisoning at a lower potential than for iron site poisoning. Hence, the limiting potential for this case is modified to $U_L' = U_O = 0.73$ V. We represent this reduction

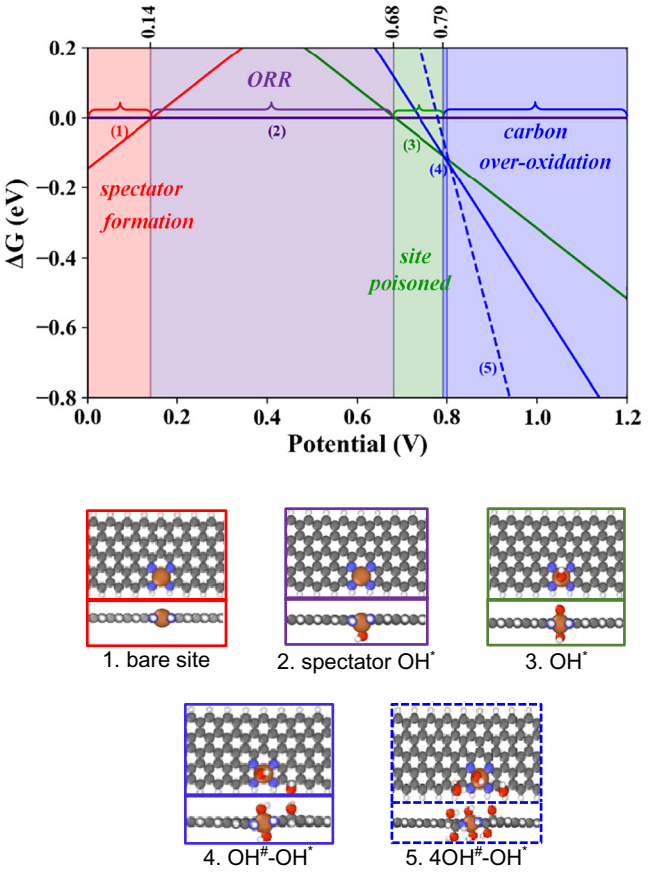

Fig. 4. Phase diagram for a pyridinic site at a zigzag edge of graphene and oxidized site configurations having OH and O groups that are energetically referenced to H_2O (top and front views). Structure 1 is a bare site configuration. Structures 2 to 5 have a spectator OH^* group. OH^* poisons the FeN_4 active site in structure 3. Structure 4 has one overoxidizing $OH^{\#}$ present on a carbon atom at the zigzag edge. Structure 5 has four $OH^{\#}$ groups, on carbon atoms along the zigzag edge surrounding OH^* on the FeN_4 site, and on each side of the graphene nanoribbon. The overoxidizing groups prefer to stay along the carbon edge next to the FeN_4 site. Structure 2 is assigned a reference energy of 0 eV. Free energies for phase transitions for every other structure by exchange of water, protons, and electrons are represented with respect to this reference phase.

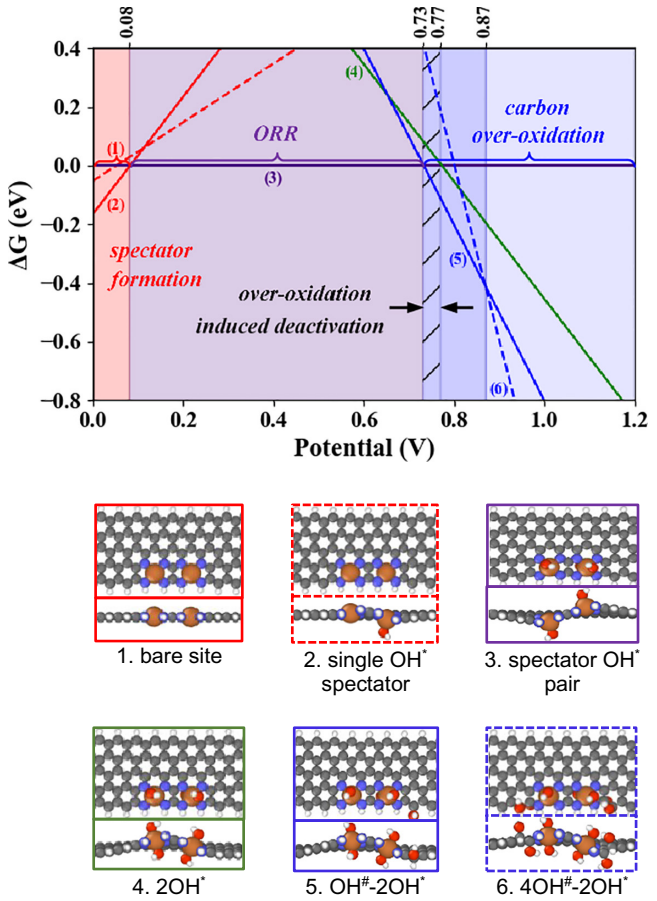

Fig. 5. Phase diagram for a pyridinic FeN_4 site pair separated by a carbon atom at the zigzag edge of graphene and oxidized site configurations having OH and O groups that are energetically referenced to H_2O (top and front views). Structure 1 is a bare site configuration. Structures 2 and 3 have $1OH^*$ and $2OH^*$ spectator groups, respectively. Structure 4 has 2 OH^* groups occupying the two iron atoms, in addition to the spectator pair. Structures 5 and 6 have overoxidizing $OH^\#$ and $4OH^\#$ groups in the vicinity of the FeN_4 sites along the zigzag edge of graphene, in addition to the 2OH* intermediates. Structure 3, with the pair of spectators, is assigned a reference energy of 0 eV. Free energies for phase transitions for every other structure by exchange of water, protons, and electrons are represented with respect to this reference phase.

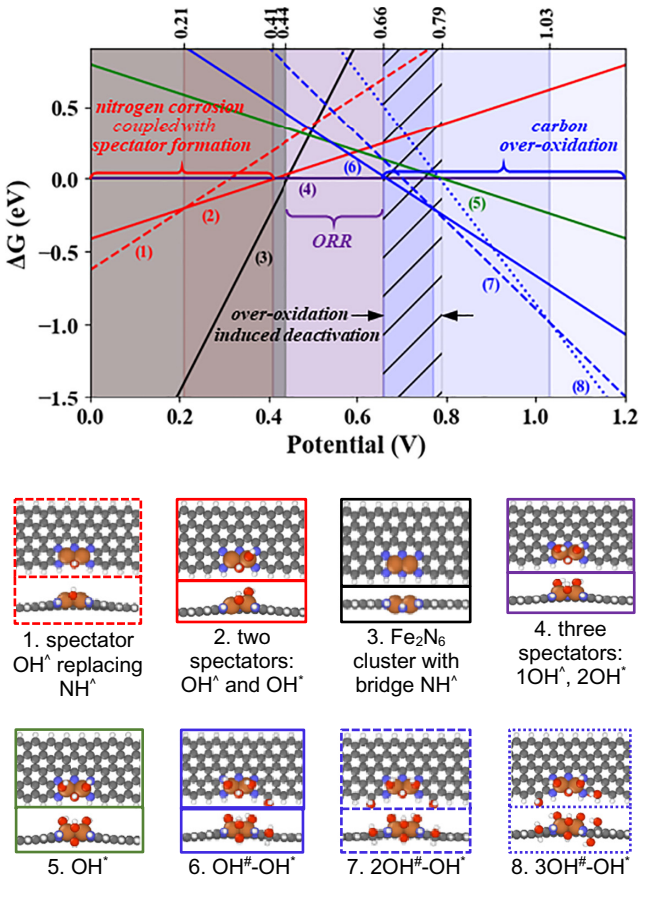

Fig. 6. Phase diagram for a clustered pyridinic Fe_2N_6 site at the zigzag edge of graphene, with oxidized site configurations having OH groups that are energetically referenced to H_2O (top and front views). Structure 3 is a bare site configuration. Structure 1 has the bridge $NH^\wedge$ replaced by a spectator $OH^\wedge$. Structures 2 and 4 have one and two additional OH^* spectators in addition to bridge $OH^\wedge$. Structure 4 is assigned a reference energy of 0 eV. Structures 5 to 8 contain OH^*, $OH^\#$-OH^*, $2OH^\#$-OH^*, and $3OH^\#$-OH^*. Free energies for phase transitions for every other structure by exchange of water, protons, and electrons are represented with respect to this reference phase.

in the ORR active potential window by a hatched region in Fig. 5, demarcated by potentials where the poisoned green structure (5) and overoxidized blue structure (6) intersect with the reference purple structure (3). These results demonstrate the importance of performing a comprehensive high coverage analysis for appropriate activity and stability predictions. We note, in passing, that intramolecular H-bonding between $OH^\#$ intermediates, away from FeN_4 sites, and OH^* on FeN_4 sites is weak and therefore does not affect overoxidation potentials. More details about the solvation stabilization are included in *SI Appendix*, section S4.2.7.

The predicted limiting potential for this site, $U_L' = 0.73$ V, is similar to that for a single FeN_4 site located at a zigzag edge ($U_L = 0.68$ V), within the uncertainty of our model. Carbon overoxidation sets in at the same potential, $U_O = 0.73$ V, indicating strong competition between ORR activity and catalyst stability.

Clustered Pyridinic Fe_2N_6 Sites at Zigzag Edge. We close by discussing clustered Fe_2N_6 sites at the zigzag edge (Fig. 1*H*). The phase diagram analysis for this site, shown in Fig. 6, indicates that the bare Fe_2N_6 site (structure 3 in black) is stable up to 0.44 V. At higher potentials, the cluster is occupied by three spectator hydroxy groups. One of these groups even replaces the NH bridging between the two iron atoms, converting the site to a Fe_2N_5 cluster. The bridge nitrogen has a driving force to undergo nitrogen corrosion and evolve $NO_{(g)}$, as per Eq. **4**:

$$NH^\wedge + 2H_2O_{(l)} \leftrightarrow OH^\wedge + NO_{(g)} + 4\left(H^+ + e^-\right), \quad [4]$$

where ^ indicates the bridge position between iron atoms where NH is bound.

NH replacement and multiple spectator formation occur simultaneously since the bare Fe_2N_6 site (structure 3) transitions directly to structure 4 (Fig. 6). Phases with a single or pair of spectator OH^* groups (structures 1 and 2, outlined in dashed and solid red), on the other hand, are not as thermodynamically favorable. After occupation of the Fe_2N_5 cluster with three spectator hydroxy groups (structure 4 in purple), ORR occurs at the second bridge position between iron atoms. This reaction can occur in a potential window between 0.44 V and $U_L = 0.79$ V, after which the site is poisoned with OH^* (structure 5 in green). A higher coverage analysis indicates that overoxidation of the neighboring carbon atom sets in with the formation of $OH^\#$-OH^* at $U_O = 0.66$ V (structure 6 in solid blue). Similar to the case of paired FeN_4 sites, overoxidation induces deactivation by lowering the limiting potential to $U_L' = U_O = 0.66$ V (depicted by a hatched region). Further increases in potential show higher degrees of overoxidized states,

with $2OH^{\#}$-OH^{*} and $3OH^{\#}$-OH^{*} (structures 7 and 8 in dashed and dotted blue) forming at 0.77 V and 1.03 V, respectively. More details of the solvation stabilization effects for the structures in this phase diagram are provided in *SI Appendix*, section S4.2.9.

In summary, a clustered Fe_2N_6 site undergoes a structural transformation, causing loss of the bridge nitrogen atom. Its predicted activity, $U_L' = 0.66$ V, is also similar to that of a single FeN_4 site at the zigzag edge ($U_L = 0.68$ V). Similar to the previous case, carbon overoxidation sets in at a potential of $U_O = 0.66$ V, indicating that, while this site exhibits good activity, its stability may be limited.

We briefly note that we have also performed a phase diagram analysis for the case where the bridge NH is retained to provide insights into the properties of Fe_2N_6. The results indicate that this Fe_2N_6 cluster is active up to $U_L = 0.69$ V and undergoes carbon overoxidation at $U_O = 0.80$ V, which are similar to the ranges of performance metrics observed for pyridinic sites. Analysis on an alternate pyridinic Fe_2N_5 configuration (Fig. 1*I*) that has also been reported to have a favorable formation energy (22) shows, however, a very low ORR activity, with $U_L = 0.20$ V. These two sites are discussed in more detail in *SI Appendix*, sections S3.5 and S3.6, respectively.

We further note that the active site configurations considered in this work correspond to regions with single graphene layers intercalated by water in the Fe-N-C catalyst. Sites could also be situated in multilayered graphitic stacks where interlayer interactions may have an additional effect, but the trends observed in single-layer models herein could still be extended to those circumstances.

We close this section by noting that Bader analyses (29) indicate that, for all site types considered, the iron atom is present in a 2+ oxidation state when the site is present in a bare configuration, which increases to 3+ in the presence of oxidizing species. Further, the Fe^{2+} bare configuration corresponds to a low/intermediate spin state, while configurations with oxidized species in Fe^{3+} configurations correspond to a low spin state for all cases except the pyrrolic FeN_4 site in large pores in the presence of a spectator OH^{*}, where the iron is observed to have an intermediate spin. The oxidation states and spin states are consistent with values expected based on isomer shifts in Mossbauer spectroscopy (20). Further, the calculated spins are consistent with trends reported previously over the pyridinic active sites in bulk graphene and pyrrolic FeN_4 large sites in pores, (20–23). Detailed descriptions of all charge and spin states are given in *SI Appendix*, section S5.

Discussion

Our thermodynamic phase diagram analyses reveal that structural evolution of active sites can be broadly categorized into four stages, as the applied potential is varied from 0 V to 1.23 V: i) spectator(s) OH formation on the underside of the Fe-N-C sheets (region in red), ii) active ORR (region in purple), iii) site poisoning (region in green), and iv) carbon overoxidation (region in yellow or blue if overoxidation results from formation of epoxy or hydroxy groups, respectively). The schematics for these stages are depicted in Fig. 7*A*.

The activity and stability insights obtained from the phase diagrams are summarized in the form of a bar plot (Fig. 7) where we additionally include results from similar analyses on pyrrolic sites (Fig. 1 *D*–*F*) and clustered Fe_2N_5 (Fig. 1*I*). Here, the active site configurations are arranged in decreasing order of intrinsic activity (shown by green bars), and the corresponding intrinsic stability for these sites is marked by the accompanying blue bars. Hatched regions in the green bars represent the reduction in the ORR active potential window induced by onset of carbon overoxidation at low potentials. The experimental half-wave potential ($E_{1/2} = 0.85$ V) and carbon dioxide onset potential ($E_{CO_2\ onset} = 0.90$ V) are marked with green and blue horizontal lines, respectively, to provide comparison with the intrinsic performance parameters.

The green bars in Fig. 7*B* indicate that pyridinic sites (1 to 5) exhibit a higher activity than pyrrolic sites (6 to 8). Among pyridinic sites, those located along a zigzag edge (1 to 3) show the highest activity, close to the experimentally observed half-wave potentials. This correspondence indicates that these structures may be the active sites responsible for driving ORR activity in Fe-N-C catalysts. A similarity in the activities of the isolated (0.68 V), paired (0.73 V), and clustered sites (0.66 V) indicates that differences in H-bonding and/or electronic structure at higher iron concentrations, do not enhance the sites' activity. Pyridinic Fe_2N_5 (9), another clustered site configuration, exhibits low activity ($U_L = 0.19$ V) owing to strong binding of hydroxyl intermediates at very low potentials, which in turn results from undercoordinated iron atoms bearing three ligating nitrogen atoms per iron, as opposed to four nitrogen atoms per iron in the case of the pyridinic Fe_2N_6 cluster (1). This result contrasts with a previous report where these sites have been proposed to exhibit a high ORR activity with a $U_L = 0.72$ V (30). The difference in conclusions is likely due to the explicit consideration of coadsorbate and solvent interactions in this work.

A significant drop is predicted in activity for armchair graphene edges (4). The activity is reduced more for in-plane defects in bulk graphene (5). The trend in relative activities of pyridinic sites at the zigzag edge and in the bulk agrees with previous reports (17). The activity remains low for pyrrolic FeN_4 sites in the bulk (6), and it is similar to their pyridinic counterparts in the bulk (5). The activity drops even further when pores are located in the vicinity of the pyrrolic sites (7, 8). This contrasts with results in some studies where pyrrolic sites (6, 7) have been proposed to exhibit higher activities for ORR than pyridinic sites (5) in the bulk of graphene (4, 31, 32). This contradiction arises because spectator groups, that we found are likely to be present under ORR conditions, were not incorporated in the previous atomistic models. An explanation of how their incorporation resolves this conflict is provided in *SI Appendix*, section S3.2. Taken together, the above results suggest that pyrrolic sites are inactive, while pyridinic FeN_4 sites at zigzag edges drive ORR activity in Fe-N-C catalysts.

Interplay between Intrinsic Activity and Intrinsic Stability. The blue bars in Fig. 7*B*, depicting intrinsic site stability, show that active sites located in the bulk have a high resistance to carbon overoxidation ($U_O > 1.20$ V). In contrast, active sites near edges (zigzag/armchair/micropore) are prone to overoxidation in potential ranges of $U_O \sim 0.7$ to 0.8 V, very close to the experimentally observed onset potential for CO_2 evolution. This result may be ascribed to a high reactivity of carbon atoms along edges, compared to the bulk, due to the undersaturation of the edge atoms. We further note that carbon atoms along a zigzag edge are overoxidized by hydroxyl groups, while armchair edges and micropores are overoxidized by epoxy groups. This difference may be due to the fact that the carbon atoms in the latter cases are more flexible and can undergo significant geometric perturbations, allowing accommodation of epoxy groups in bridge positions. The overoxidized states that we have identified, from phase diagrams at potentials corresponding to U_O, are shown in Fig. 7*C*. These structures may provide precursor states for carbon corrosion.

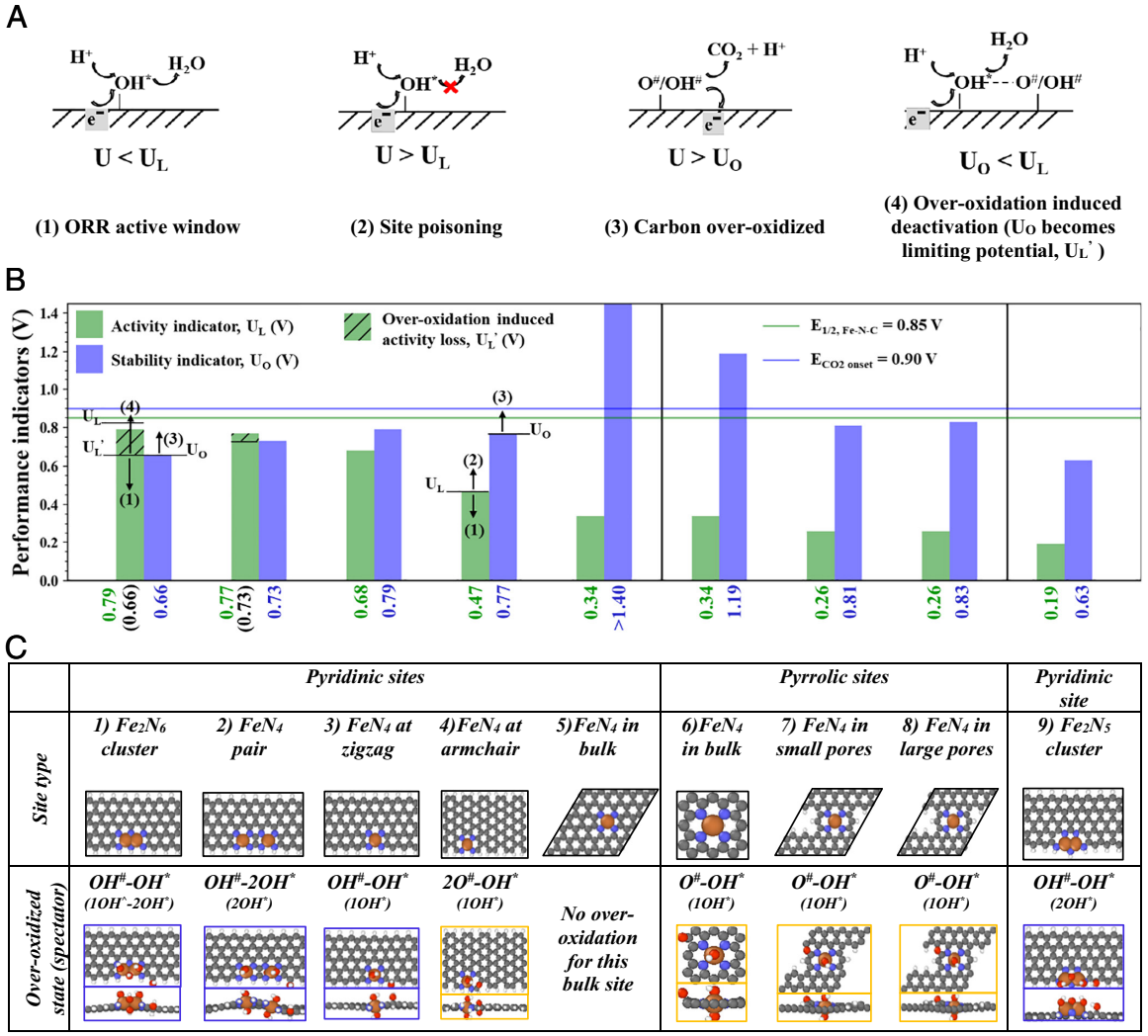

Fig. 7. (*A*) Schematic depicting ORR, site poisoning, carbon corrosion after carbon overoxidation, and overoxidation-induced deactivation as a function of potential, and (*B*) performance indicators for various FeN_x moieties in the Fe-N-C catalyst. Limiting potentials, U_L, (green bars) indicate activity, while overoxidation potentials, U_O (blue bars), represent stability, with their respective values denoted at the bottom of the bar plot. (*C*) Corresponding atomistic models are shown below the bar plots, with unit cells outlined in black. Configurations where overoxidation of the neighboring carbon atoms occurs at U_O are also shown ("*" and "#" represent iron and carbon as binding sites, respectively, and "^" represents the bridge position in the iron cluster where $OH^\wedge$ replaced an $NH^\wedge$). Overoxidation is caused either by hydroxy or epoxy groups, outlined in blue and yellow, respectively. These groups may be precursor states for carbon corrosion. A given site poisons above U_L; hence, a high U_L indicates high intrinsic activity, while carbon overoxidation occurs above U_O, which can lead to carbon corrosion. Thus, a high U_O indicates high intrinsic site stability. In some cases, carbon overoxidation induces deactivation by lowering the site poisoning potential (if $U_O < U_L$). In this case, the site activity drops to $U_L' = U_O$ from U_L, with the decline denoted by the hatched region in the green bars. The experimentally observed ORR half-wave potential ($E_{1/2}$ = 0.85V) is plotted as a horizontal green line, providing a direct comparison with intrinsic site activity predicted from U_L. Similarly, the experimental CO_2 onset potential ($E_{1/2}$ = 0.90V) is plotted as a horizontal blue line, providing a comparison with the intrinsic site stability predicted from U_O.

The combined activity and selectivity results imply that, for the pyridinic FeN_4 sites along the zigzag edge (1 to 3), the potential windows for ORR and overoxidation are similar. Hence, the retention of site activity could be affected by deactivation via interaction of overoxidized groups with the intermediates, as is evident from the cases of clustered Fe_2N_6 (1) and paired FeN_4 (2) sites, where overoxidation is predicted to be problematic above 0.66 and 0.73 V, respectively. These potentials overlap with the predicted active region for the ORR (below 0.79 and 0.77 V). The difference between the values corresponds to the loss of active voltage induced by overoxidation, which is depicted by the hatched region in the green bars. The high driving force for carbon overoxidation, compared to ORR, could also lead to site loss initiated by carbon corrosion at the overoxidized edge carbons for these sites, indicating that they may be less stable than the isolated pyridinic FeN_4 site (1). Future investigations of the kinetics of the competition between ORR and carbon corrosion would be very desirable. In general, the results also point to an inverse relation between activity and stability, where sites such as pyridinic FeN_4 in the bulk, with low predicted activities (short green bars), are less sensitive to carbon overoxidation (high blue bars).

Conclusions

Extensive structural analyses were performed for a comprehensive set of active sites that can form in single layers of graphene in Fe-N-C catalysts. The structures of the active sites are modified under reaction conditions in the presence of water, with high coverages of hydroxyl groups sometimes forming as either spectator species or precursors to carbon overoxidation. Incorporation of rigorous solvation corrections, dependent on the hydroxyl coverages, is central to the analysis, as these corrections do not scale linearly with the number of surface hydroxyl groups. In general, pyridinic sites at zigzag edges exhibit the highest activities for

ORR. However, even though these sites have the highest predicted activities for the ORR, carbon atoms at the zigzag edges are prone to overoxidation, raising stability concerns for the active sites. Clustering of sites appears to enhance activity, but these sites are again vulnerable to deactivation due to carbon overoxidation. The precise mechanism by which overoxidation affects the kinetics of the ORR landscape is not discussed here but will be described in a future study. Once the neighboring carbon atoms become overoxidized, it is quite plausible that, over many fuel cell potential cycles, highly oxidized sites could be susceptible to permanent deactivation via mechanisms such as carbon corrosion (11–13). Since carbon atoms near the FeN_x sites are most vulnerable to oxidation, it is also plausible that carbon corrosion originating at these locations in turn accelerates site loss by metal leaching (11, 14). The high coverage structures identified here thus provide precursor states from which potential-dependent degradation mechanisms proceed and may be used in subsequent kinetic analyses. Hence, we conclude that carbon overoxidation limits ORR activity of sites and enforces a narrow potential window in which ORR can occur. Controls to avoid voltage spikes during fuel cell operations are needed so as to prevent carbon corrosion and site loss at highly oxidizing potentials. Since active sites in the bulk do not raise any stability concerns, however, it may also be worthwhile to work toward enhancing their activity via strategies such as doping.

Materials and Methods

Active sites in the Fe-N-C catalyst are modeled by multiple configurations, shown in Fig. 1, in a single graphene sheet or a nanoribbon in vacuum, with an interlayer spacing of 20 Å to avoid periodic interactions. Structures with epoxy or hydroxy intermediates in all possible unique positions over iron, carbon, or nitrogen atoms, illustrated in *SI Appendix*, Fig. S1, and their combinations at high coverages, are enumerated with SurfGraph (27). All structures are relaxed with periodic density functional theory (DFT), and the minimum energy configuration is determined at every coverage. Spin-polarized calculations for structure optimization are performed using VASP (Vienna Ab-initio Simulation Package) in a planewave basis set (33, 34). A planewave cutoff energy of 400 eV and a Monkhorst-Pack K point (33, 35) grid spacing of 3 × 3 × 1 are chosen for all active sites after convergence tests. BEEF-vdW (Bayesian error estimation functional with van der Waals correlation) (36–38), a type of GGA (generalized gradient approximation) exchange correlation functional (39), is used to model the electron interactions, and projector augmented wave (PAW) pseudopotentials (40) are used to represent core electrons in the DFT calculations. The energy convergence limit is set to 10^{-5} eV/atom, with a force convergence criterion of 0.03 eV/Å. Structures are relaxed at different initial guesses of overall magnetic moments, and the resulting minimum energy structures are used for all analyses. In particular, the spins on the iron atoms, corresponding to the magnetic moment of the iron, are calculated and reported in *SI Appendix*, Table S8 for the minimum energy structures. Further, the charges on the iron atoms with different adsorbate configurations are determined from Bader analyses (29) and are reported in *SI Appendix*, Table S6. All calculations are carried out with the atomic simulation environment (ASE) python interface (41).

Corrections to account for the stabilizing effect of solvation of OH^* intermediates in an aqueous environment are added to the energies obtained for structures in vacuum. These are determined with an in-house formalism (42) based on ab initio molecular dynamics (AIMD) simulations with explicit water molecules for different active site configurations, as discussed in *SI Appendix*, section S4.

Data, Materials, and Software Availability. All study data are included in the article and/or *SI Appendix*.

ACKNOWLEDGMENTS. Financial support from the Department of Energy Office of Science, Office of Basic Energy Sciences, Chemical, Biological, and Geosciences Division under DE-SC0010379, is gratefully acknowledged. Use of the Center for Nanoscale Materials, a US Department of Energy, Office of Science, Office of Basic Energy Sciences User Facility under Contract No. DE-AC02-06CH11357, and of computational resources from the National Energy Research Scientific Computing Center is also acknowledged.

1. F. Jaouen *et al.*, Recent advances in non-precious metal catalysis for oxygen-reduction reaction in polymer electrolyte fuelcells. *Energy Environ. Sci.* **4**, 114–130 (2011), 10.1039/C0EE00011F.
2. G. Wu, K. L. More, C. M. Johnston, P. Zelenay, High-performance electrocatalysts for oxygen reduction derived from polyaniline, iron, and cobalt. *Science* **332**, 443–447 (2011), 10.1126/science.1200832.
3. A. Mehmood *et al.*, High loading of single atomic iron sites in Fe–NC oxygen reduction catalysts for proton exchange membrane fuel cells. *Nat. Catal.* **5**, 4 (2022), 10.1038/s41929-022-00772-9.
4. S. Liu *et al.*, Atomically dispersed iron sites with a nitrogen–carbon coating as highly active and durable oxygen reduction catalysts for fuel cells. *Nat. Energy* **7**, 7 (2022), 10.1038/s41560-022-01062-1.
5. S. T. Thompson *et al.*, Direct hydrogen fuel cell electric vehicle cost analysis: System and high-volume manufacturing description, validation, and outlook. *J. Power Sources* **399**, 304–313 (2018), 10.1016/j.jpowsour.2018.07.100.
6. M. Winter, R. J. Brodd, What are batteries, fuel cells, and supercapacitors? *Chem. Rev.* **104**, 4245–4270 (2004), 10.1021/cr020730k.
7. R. P. O'Hayre, S.-W. Cha, W. G. Colella, F. B. Prinz, *Fuel Cell Fundamentals* (Wiley, Hoboken, New Jersey, ed. 3, 2016).
8. B. Pivovar, Catalysts for fuel cell transportation and hydrogen related uses. *Nat. Catal.* **2**, 562–565 (2019), 10.1038/s41929-019-0320-9.
9. C. H. Choi *et al.*, The Achilles' heel of iron-based catalysts during oxygen reduction in an acidic medium. *Energy Environ. Sci.* **11**, 3176–3182 (2018), 10.1039/C8EE01855C.
10. V. Goellner, V. Armel, A. Zitolo, E. Fonda, F. Jaouen, Degradation by hydrogen peroxide of metal-nitrogen-carbon catalysts for oxygen reduction. *J. Electrochem. Soc.* **162**, H403–H414 (2015), 10.1149/2.1091506jes.
11. C. H. Choi *et al.*, Stability of Fe-N-C catalysts in acidic medium studied by operando spectroscopy. *Angew. Chem. Int. Ed.* **54**, 12753–12757 (2015), 10.1002/anie.201504903.
12. E. F. Holby, First-principles molecular dynamics study of carbon corrosion in PEFC catalyst materials. *Fuel. Cells* **16**, 669–674 (2016), 10.1002/fuce.201600012.
13. V. Goellner *et al.*, Degradation of Fe/N/C catalysts upon high polarization in acid medium. *Phys. Chem. Chem. Phys.* **16**, 18454–18462 (2014), 10.1039/C4CP02882A.
14. C. H. Choi *et al.*, Minimizing operando demetallation of Fe-N-C electrocatalysts in acidic medium. *ACS Catal.* **6**, 3136–3146 (2016), 10.1021/acscatal.6b00643.
15. J. Herranz *et al.*, Unveiling N-protonation and anion-binding effects on Fe/N/C catalysts for O_2 reduction in proton-exchange-membrane fuel cells. *J. Phys. Chem. C* **115**, 16087–16097 (2011), 10.1021/jp2042526.
16. I. Matanovic, K. Artyushkova, P. Atanassov, Understanding PGM-free catalysts by linking density functional theory calculations and structural analysis: Perspectives and challenges. *Curr. Opin. Electrochem.* **9**, 137–144 (2018), 10.1016/j.coelec.2018.03.009.
17. H. T. Chung *et al.*, Direct atomic-level insight into the active sites of a high-performance PGM-free ORR catalyst. *Science* **357**, 479–484 (2017), 10.1126/science.aan2255.
18. S. Kabir, K. Artyushkova, A. Serov, B. Kiefer, P. Atanassov, Binding energy shifts for nitrogen-containing graphene-based electrocatalysts - experiments and DFT calculations: Analyzing structure-property relationships of functionalized materials. *Surface Interface Anal.* **48**, 293–300 (2016), 10.1002/sia.5935.
19. U. I. Kramm *et al.*, Structure of the catalytic sites in Fe/N/C-catalysts for O2-reduction in PEM fuel cells". *Phys. Chem. Chem. Phys.* **14**, 11673 (2012), 10.1039/c2cp41957b.
20. T. Mineva *et al.*, Understanding active sites in pyrolyzed Fe–N–C catalysts for fuel cell cathodes by bridging density functional theory calculations and ^{57} Fe Mössbauer spectroscopy. *ACS Catal.* **9**, 9359–9371 (2019), 10.1021/acscatal.9b02586.
21. J. Li *et al.*, Identification of durable and non-durable FeNx sites in Fe–N–C materials for proton exchange membrane fuel cells. *Nat. Catal.* **4**, 1 (2021), 10.1038/s41929-020-00545-2.
22. L. Ni *et al.*, Identification of the catalytically dominant iron environment in iron- and nitrogen-doped carbon catalysts for the oxygen reduction reaction. *J. Am. Chem. Soc.* **144**, 16827–16840 (2022), 10.1021/jacs.2c04865.
23. M. Primbs *et al.*, Establishing reactivity descriptors for platinum group metal (PGM)-free Fe–N–C catalysts for PEM fuel cells. *Energy Environ. Sci.* **13**, 2480–2500 (2020), 10.1039/D0EE01013H.
24. S. Kattel, P. Atanassov, B. Kiefer, A density functional theory study of oxygen reduction reaction on non-PGM Fe–Nx–C electrocatalysts. *Phys. Chem. Chem. Phys.* **16**, 13800 (2014), 10.1039/c4cp01634c.
25. S. Kabir, K. Artyushkova, B. Kiefer, P. Atanassov, Computational and experimental evidence for a new TM–N_3/C moiety family in non-PGM electrocatalysts. *Phys. Chem. Chem. Phys.* **17**, 17785–17789 (2015), 10.1039/C5CP02230D.
26. E. F. Holby, G. Wu, P. Zelenay, C. D. Taylor, Structure of Fe–Nx –C defects in oxygen reduction reaction catalysts from first-principles modeling. *J. Phys. Chem. C* **118**, 14388–14393 (2014), 10.1021/jp503266h.
27. S. Deshpande, T. Maxson, J. Greeley, Graph theory approach to determine configurations of multidentate and high coverage adsorbates for heterogeneous catalysis, *npj Comput. Mater.* **6**, 1 (2020), 10.1038/s41524-020-0345-2.
28. J. K. Nørskov *et al.*, Origin of the overpotential for oxygen reduction at a fuel-cell cathode. *J. Phys. Chem. B* **108**, 17886–17892 (2004), 10.1021/jp047349j.
29. W. Tang, E. Sanville, G. Henkelman, A grid-based Bader analysis algorithm without lattice bias. *J. Phys. Condens. Matter* **21**, 084204 (2009), 10.1088/0953-8984/21/8/084204.
30. E. F. Holby, C. D. Taylor, Activity of N-coordinated multi-metal-atom active site structures for Pt-free oxygen reduction reaction catalysis: Role of *OH ligands. *Sci. Rep.* **5**, 9286 (2015), 10.1038/srep09286.
31. F. Calle-Vallejo, J. I. Martínez, J. Rossmeisl, Density functional studies of functionalized graphitic materials with late transition metals for oxygen reduction reactions. *Phys. Chem. Chem. Phys.* **13**, 15639 (2011), 10.1039/c1cp21228a.
32. K. Liu, G. Wu, G. Wang, Role of local carbon structure surrounding FeN_4 sites in boosting the catalytic activity for oxygen reduction. *J. Phys. Chem. C* **121**, 11319–11324 (2017), 10.1021/acs.jpcc.7b00913.

33. W. Kohn, L. J. Sham, Self-consistent equations including exchange and correlation effects. *Phys. Rev.* **140**, A1133–A1138 (1965), 10.1103/PhysRev.140.A1133.
34. G. Kresse, J. Furthmüller, Efficient iterative schemes for *ab initio* total-energy calculations using a plane-wave basis set. *Phys. Rev. B* **54**, 11169–11186 (1996), 10.1103/PhysRevB.54.11169.
35. H. J. Monkhorst, J. D. Pack, Special points for Brillouin-zone integrations. *Phys. Rev. B* **13**, 5188–5192 (1976), 10.1103/PhysRevB.13.5188.
36. J. Wellendorff *et al.*, Density functionals for surface science: Exchange-correlation model development with Bayesian error estimation. *Phys. Rev. B* **85**, 235149 (2012), 10.1103/PhysRevB.85.235149.
37. J. Klimeš, D. R. Bowler, A. Michaelides, Chemical accuracy for the van der Waals density functional. *J. Phys. Condens Matter.* **22**, 022201 (2010), 10.1088/0953-8984/22/2/022201.
38. J. Klimeš, D. R. Bowler, A. Michaelides, Van der Waals density functionals applied to solids. *Phys. Rev. B* **83**, 195131 (2011), 10.1103/PhysRevB.83.195131.
39. P. E. Blöchl, Projector augmented-wave method. *Phys. Rev. B* **50**, 17953–17979 (1994), 10.1103/PhysRevB.50.17953.
40. G. Kresse, D. Joubert, From ultrasoft pseudopotentials to the projector augmented-wave method. *Phys. Rev. B* **59**, 1758–1775 (1999), 10.1103/PhysRevB.59.1758.
41. A. Hjorth Larsen *et al.*, The atomic simulation environment–a Python library for working with atoms. *J. Phys. Condens. Matter.* **29**, 273002 (2017), 10.1088/1361-648X/aa680e.
42. H. Chun, A. Morankar, Z. Zeng, J. Greeley, Solvation enthalpy determination for aqueous-phase reaction adsorbates from first principles ab initio molecular dynamics, ChemRxiv [Preprint] (2023). https://doi.org/10.26434/chemrxiv-2023-mxdcf (Accessed 17 May 2023).